RESEARCH ARTICLE | FEBRUARY 14 2025

Interaction between acoustics and flame dynamics in a multi-element liquid rocket engine: Mode switching via quasi-periodic oscillation

Yuanzhe Liu (刘远哲); Zhuopu Wang (王琢璞) ; Xiaoxin Wu (武晓欣); Yu Guan (关昱) ; Zhuyin Ren (任祝寅) ; Peijin Liu (刘佩进)

Physics of Fluids 37, 025180 (2025)
https://doi.org/10.1063/5.0253498

Physics of Fluids ARTICLE pubs.aip.org/aip/pof

Interaction between acoustics and flame dynamics in a multi-element liquid rocket engine: Mode switching via quasi-periodic oscillation

Cite as: Phys. Fluids **37**, 025180 (2025); doi: 10.1063/5.0253498
Submitted: 17 December 2024 · Accepted: 17 January 2025 ·
Published Online: 14 February 2025

Yuanzhe Liu (刘远哲),[1] Zhuopu Wang (王琢璞),[2,a)] Xiaoxin Wu (武晓欣),[2,3] Yu Guan (关昱),[4] Zhuyin Ren (任祝寅),[1] and Peijin Liu (刘佩进)[2]

AFFILIATIONS

[1]Institute for Aero Engine, Tsinghua University, Beijing 100084, China
[2]Science and Technology on Combustion, Internal Flow and Thermal-Structure Laboratory, Northwestern Polytechnical University, Xi'an 710072, China
[3]Xi'an Aerospace Propulsion Institute, Xi'an 710100, China
[4]Department of Aeronautical and Aviation Engineering, The Hong Kong Polytechnic University, Kowloon, Hong Kong

[a)]Author to whom correspondence should be addressed: zpwang@nwpu.edu.cn

ABSTRACT

This study presents the first numerical evidence of mode switching via quasi-periodic oscillations in a self-excited thermoacoustic system—model multi-element liquid rocket combustor burning methane and hydrogen peroxide—by varying the global equivalence ratio ($1.7 \leq \phi \leq 0.3$). We employed a full-scale, three-dimensional compressible Detached Eddy Simulation in OpenFOAM, coupled with the partially stirred reactor turbulent combustion model, and modeled chemical reactions with a global two-step reaction mechanism to account for finite-rate chemistry. The methane mass flow rate is systematically reduced to explore three main aspects: (1) dynamical bifurcations in the thermoacoustic system, (2) the coupling between pressure and the combustion fields, and (3) the evolution of flame dynamics, including mixing and combustion modes. Results reveal multiple bifurcations and mode switching. For $1.7 \leq \phi \leq 0.5$, the system shows simple period-1 limit cycle oscillations dominated by the first longitudinal (1L) acoustic mode. As ϕ decreases to 0.3, the system transitions to a low-amplitude limit cycle state dominated by the second transverse (2T) acoustic mode. At $\phi = 0.4$, interactions between multiple acoustic modes (1L, 2T) and non-acoustic mode induce a quasi-periodic state with three periods. Frequency-locking is identified as the mechanism driving mode switching, and the spatial distribution of premixed and diffusion flames, analyzed through the Flame Index, is shown to be critical in this process.

I. INTRODUCTION

Despite extensive efforts to mitigate it, thermoacoustic instability (TAI) remains a critical challenge in liquid rocket propulsion systems.[1–3] When TAI occurs in the combustion chamber, it induces large-amplitude periodic acoustic oscillations that can lead to catastrophic mechanical damage and mission failure.[4] A notable example is the F-1 engine, which powered the Saturn rockets during the Apollo lunar missions and suffered severe transverse TAI.[5] The instability was significant, with acoustic pressure oscillation amplitudes exceeding twice the intended operational level. In response, "Project First" was initiated—a four-year research program comprising preliminary flight rating tests, flight rating tests, and flight qualification tests. This program tested 108 injector types across 1332 experiments, marking a groundbreaking milestone in understanding and suppressing transverse TAI through passive measures like installing baffles.[6] Despite these advancements, a comprehensive understanding of the physical mechanisms driving TAI remains elusive, attracting significant worldwide research attention. TAI is commonly attributed to a positive feedback loop involving the interaction of turbulent flow, unsteady combustion heat release, and acoustic pressure oscillation within the combustion chamber.[7] The driving mechanisms can be highly complex, varying with engine geometry and operating conditions. In liquid rocket engines with coaxial injection elements, two primary instability mechanisms are observed: (1) resonance phenomena due to coupling between the acoustic cavity of the coaxial injector and the combustion chamber[8] and (2) large-scale vortex structures formed from flow

separation near the dump plane, which, when ignited by hot products, induce small-scale turbulence and oscillatory heat release.[9,10] This paper aims to investigate TAI phenomena and underlying physical mechanisms in a multi-element liquid rocket engine with coaxial injection elements.

The propagation of acoustic waves in the combustion chamber is characterized by high nonlinearity. During TAI, acoustic disturbances typically exhibit exponential growth within a linear framework. However, practical systems eventually reach a limit cycle state with finite amplitude due to nonlinear effects like flame response and aerodynamic characteristics.[4,11] Traditionally, dynamical systems theory posits that thermoacoustic systems exhibit limit cycle states (TAI) or fixed point states (FP, combustion noise).[12,13] Limit cycle states are characterized by a single frequency and constant amplitude, with primary energy transfer between a single acoustic mode and heat release. Recent research has revealed more complex dynamical states, such as intermittency, period-n oscillations, quasiperiodicity, and chaos, indicating that limit cycles are just one possible outcome of TAI. The coexistence and interaction of multiple acoustic modes lead to complex nonlinear dynamics, but these phenomena remain poorly understood. Multiple bifurcations in thermoacoustic systems, influenced by varying operational conditions (e.g., global equivalence ratio, reactant temperature), have garnered attention. For instance, simple laminar thermoacoustic systems can exhibit a range of oscillatory behaviors, from P1 oscillations to quasi-periodic and chaotic states.[14–16] In liquid rocket engines, complex turbulent motion coupled with unsteady combustion introduces additional degrees of freedom. Sujith and colleagues[17–19] observed a bifurcation process from intermittency to TAI in a two-dimensional liquid rocket combustor, suggesting a transition paradigm (FP → intermittency → P1) distinct from traditional Hopf bifurcation (FP → P1). Intermittency here signifies spontaneous transitions in system dynamics between FP and P1. From a nonlinear prediction perspective, Aoki *et al.*[20] studied intermittent combustion oscillations in atmospheric rocket combustors, utilizing symbolic dynamics and graph networks. In the previous work, we systematically discussed the emergence of multiple bifurcation processes with varying control parameters. These studies were numerically performed in (1) a single-element rocket combustor burning hydrogen peroxide and methane,[21,22] (2) a single-element rocket combustor burning hydrogen peroxide and liquid kerosene,[23,24] and (3) a multi-element rocket combustor burning hydrogen peroxide and methane.[25] These multiple bifurcation processes led to complex nonlinear states, including FP, limit cycles (P1), period-2 (P2), and intermittency. However, reports of quasiperiodicity and chaos in liquid rocket engines remain sparse.

Quasiperiodic oscillations, resulting from the interaction of at least two incommensurate frequencies, are a complex nonlinear phenomenon where the phase space trajectory never exactly repeats. In self-excited thermoacoustic systems, quasiperiodicity can arise from the competition between natural modes. While quasiperiodic oscillations have been observed in ducted premixed flames near the lean blowout limit over a specific range of flame positions,[15,16] they have not been reported in liquid rocket combustors. This paper presents numerical evidence of mode switching via quasi-periodic oscillations in a model multi-element liquid rocket combustor as we vary the global equivalence ratio. Mode switching refers to the transition between natural modes in response to time or control parameter changes.[26] To address these issues, this paper employs a comprehensive three-dimensional detached Eddy simulation (DES) method combined with a multi-step finite-rate chemical reaction kinetics mechanism to investigate bifurcation processes in a multi-element liquid rocket engine burning hydrogen peroxide and methane. The engine features five coaxial shear injectors, a combustion chamber, and a short nozzle. The study adjusts the methane mass flow rate, varying the global equivalence ratio from 1.7 to 0.3, encompassing both fuel-rich and oxygen-rich combustion cycles. The oxidizer, hydrogen peroxide at 90% mass concentration, produces 58% water vapor and 42% oxygen at high temperature (1030 K) in the catalytic bed, while methane is used as the fuel at room temperature (300 K). These operating conditions replicate those of the continuous variable resonance combustor (CVRC) experimental setup designed by Purdue University.[27–29] This work extends the computational domain from single to multi-element designs, enhancing injector jet coupling and reducing the length-to-diameter ratio, potentially inducing transverse instability. The study explores bifurcation processes within the global equivalence ratio parameter space, utilizing linear and nonlinear time series analysis methods [e.g., fast Fourier transform (FFT), short time Fourier transform (STFT), phase space trajectories, and recurrence plots (RP)] to uncover nonlinear dynamics. Additionally, it examines spatiotemporal combustion flow field evolution using parameters like mixture fraction and flame index (FI) to reveal flame dynamics and mixing dynamics.

II. PHYSICAL MODEL

The three-dimensional computational domain features five coaxial injectors, a combustion chamber, and a short nozzle connected at the end. The simulation is based on an extension of the continuous variable resonant chamber (CVRC) test rig, a single-element model liquid rocket engine previously developed by Anderson's team at Purdue University.[27] The number of injectors in this system was expanded from a single coaxial shear injector to five coaxial shear injectors, where the injector size was consistent with the CVRC. The chamber has a diameter of 11.4 cm and a length of 38.1 cm. Each injector has a central oxidizer post that is 15 cm long with a diameter of 2.05 cm. Methane is introduced through an annular gap surrounding this post: inner annular gap (diameter of 2.2 cm), outer annular gap (diameter of 2.3 cm), and an internal access of 1 cm in length supports the pre-mixing of fuel and oxidizer. The nozzle has an area ratio of 1:5 relative to the combustion chamber. Figures 1(b) and 1(c) illustrate the mesh near the dump plane and the short nozzle, respectively. A structured hexahedral mesh was used in the three-dimensional domain to ensure orthogonality and reduce computational cost. The mesh consists of approximately 9.2×10^6 hexahedral cells, with the smallest cell size being less than 0.1 mm. To ensure result accuracy, a mesh independence study will be conducted in Sec. III C.

Hydrogen peroxide and methane are used as the oxidizer and fuel, respectively. Hydrogen peroxide, with a mass concentration of 90%, is dissociated into 42% oxygen and 58% water vapor at 1030 K after passing through a high-temperature catalytic bed before entering the oxidizer post. Methane, at room temperature (300 K), is introduced through the fuel injector. The total mass flow rates are 0.135 kg/s for fuel and 1.5 kg/s for oxidizer, resulting in oxygen-rich combustion with a global equivalence ratio of 0.8. Such operating conditions have

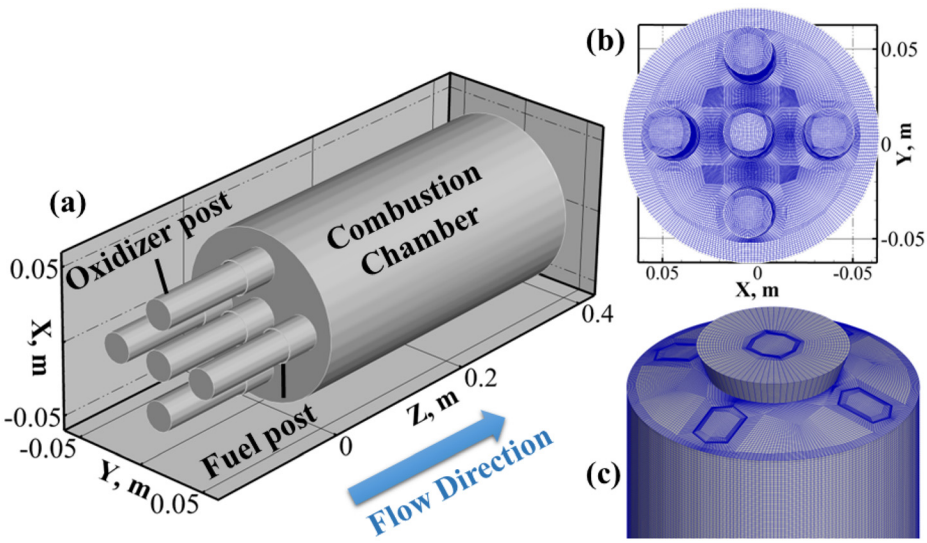

FIG. 1. (a) Schematic diagram of the three-dimensional geometry, (b) block-structured local mesh near the dump plane, and (c) block-structured local mesh near the nozzle.[25]

recently been widely applied in simulating the thrust chambers of oxygen-rich staged cycle (ORSC) engines. The designed combustor pressure is approximately 1.3 MPa. The CVRC experimental operating condition was designed to simplify combustion dynamics by eliminating processes, such as atomization and evaporation. As Professor William A. Sirignano[30] noted, although the CVRC experiment employs gaseous injection, it serves as an accepted benchmark for computational methods addressing combustion instability in Liquid Propellant Rocket Engines. Furthermore, when the preheated reactant temperature significantly exceeds the critical temperature of the species, neglecting real gas effects is acceptable in engineering calculations. Consequently, simulations conducted under subcritical conditions can provide reference values applicable to supercritical pressure conditions to a reasonable extent in real engines. A two-step methane/oxygen finite-rate chemical reaction kinetics mechanism is employed. This mechanism is detailed in Table I and involves six species with two-step reaction kinetics: An irreversible reaction and A reversible reaction, leading to equilibrium between CO and CO_2. Initially developed for methane/air turbulent flames, this reaction mechanism has been effectively used in recent simulations of turbulent combustion instability in hydrogen peroxide/methane systems.[31,32]

III. NUMERICAL METHODOLOGY

A. Governing equations and sub-grid models

The governing equations for compressible turbulent reactive flow of a multi-species gas mixture are the three-dimensional Navier–Stokes equations, which include mass conservation, momentum conservation, energy conservation, and species transport. The Favre-filtered governing equations are expressed as

$$\frac{\partial \overline{\rho}}{\partial t}+\frac{\partial \overline{\rho}\widetilde{u}_j}{\partial x_j}=0, \tag{1}$$

$$\frac{\partial \overline{\rho}\widetilde{u}_j}{\partial t}+\frac{\partial\left(\overline{\rho}\widetilde{u}_i\widetilde{u}_j\right)}{\partial x_i}+\frac{\partial \overline{p}}{\partial x_j}=\frac{\partial\left(\overline{\tau}_{ij}-\overline{\rho}\left(\widetilde{u_iu_j}-\widetilde{u}_i\widetilde{u}_j\right)\right)}{\partial x_i}, \tag{2}$$

$$\frac{\partial \overline{\rho}\widetilde{h}_s}{\partial t}+\frac{\partial\left(\overline{\rho}\widetilde{u}_i\widetilde{h}_s\right)}{\partial x_i}=\frac{\overline{Dp}}{Dt}+\frac{\partial}{\partial x_i}\left[\overline{\lambda\frac{\partial T}{\partial x_i}}-\overline{\rho}\left(\widetilde{u_ih_s}-\widetilde{u}_i\widetilde{h}_s\right)\right]+\overline{\tau_{ij}\frac{\partial u_i}{\partial x_j}}-\frac{\partial}{\partial x_i}\left(\overline{\rho\sum_{k=1}^{N}V_{k,i}Y_kh_{s,k}}\right)+\overline{\dot{S}}_{energy}, \tag{3}$$

$$\frac{\partial\left(\overline{\rho}\widetilde{Y}_k\right)}{\partial t}+\frac{\partial\left(\overline{\rho}\widetilde{u}_i\overline{Y}_k\right)}{\partial x_i}=\frac{\partial}{\partial x_i}\left[\overline{V_{k,i}Y}_k-\overline{\rho}\left(\widetilde{u_iY}_k-\widetilde{u}_i\widetilde{Y}_k\right)\right]+\overline{\dot{S}}_{species}\ k=1,N. \tag{4}$$

Here, Favre-filtered quantities are denoted with a tilde (-), and terms with superscript (∼) denote the contributions from the subgrid scales (SGS). The variables ρ, u_j, p, h_s, and Y_k represent the density, velocity component in the j-direction, pressure, specific enthalpy, and mass fraction of species-k, respectively. The stress tensor is denoted by τ_{ij}. The terms $\overline{\dot{S}}_{energy}$ and $\overline{\dot{S}}_{species}$ correspond to the source terms arising from chemical reactions. The term $V_{k,i}Y_k$ indicates the laminar diffusion flux. The stress tensor τ_{ij} for a multi-species gas mixture is formulated as

TABLE I. The mechanism of chemical reaction kinetics.[25]

Chemical reactions	A, s^{-1}	Ea, J/(kg mol)	nCH_4	nO_2	nCO_2	nCO
$CH_4+1.5O_2\rightarrow CO+2H_2O$	2.0×10^{15}	34 500	0.9	1.1		
$CO+0.5O_2\rightleftharpoons CO_2$	2.0×10^{9}	12 000		0.5	1	1

$$\tau_{ij} = -\mu\left(\frac{\partial u_i}{\partial x_j} + \frac{\partial u_j}{\partial x_i} - \frac{2}{3}\delta_{ij}\frac{\partial u_k}{\partial x_k}\right) - \mu_t\left(\frac{\partial u_i}{\partial x_j} + \frac{\partial u_j}{\partial x_i} - \frac{2}{3}\delta_{ij}\frac{\partial u_k}{\partial x_k}\right) + \tau_{ij}^{sgs}, \quad (5)$$

where μ denotes the dynamical viscosity coefficient, μ_t stands for the turbulent viscosity, δ_{ij} represents the Kronecker delta function, and τ_{ij}^{sgs} signifies the sub-grid scale stress tensor. For the diffusion flux, assuming a Lewis number of unity ($Le = 1$), the expression is given by

$$\overline{V_{k,i}Y_k} = -\overline{\rho}\overline{D}_k\frac{\partial_i\widetilde{Y}_k}{\partial x_i}, \quad (6)$$

where D_k denotes the molecular diffusion coefficient for species k.

In the detached Eddy simulation (DES) approach, unsteady Reynolds-averaged Navier–Stokes (RANS) models are used for the boundary layer, while large Eddy simulation (LES) is applied to separated flow regions, typically associated with core turbulent zones where large-scale turbulence motion dominates. In these zones, DES models simulate LES-like subgrid models. Conversely, near-wall regions revert to the corresponding RANS models. This study employs a DES model based on the k–ω SST model, which has recently been applied to simulate combustion instability in liquid rocket engines with good accuracy.[25,33] Additionally, the partially stirred reactor (PaSR) model is used to account for the coupling between turbulence and finite-rate chemical reactions, showing excellent performance in simulating partially premixed combustion under various engine operating conditions.[32,34,35]

B. Boundary conditions and initial conditions

At the oxidizer and fuel inlets, Dirichlet boundary conditions with constant mass flow rates are applied. Since the flow at the nozzle exit is supersonic, wave-transmissive boundary conditions are employed at the exit to prevent acoustic wave reflections from reentering the combustion chamber. The walls are treated as no-slip, impermeable, and adiabatic, ensuring no heat or mass transfer occurs through them. Zero-gradient pressure boundary conditions, acting as rigid acoustic boundaries, are applied at both the oxidizer and fuel inlets. Similarly, the walls serve as rigid acoustic boundaries, with no acoustic energy loss assumed. This adiabatic wall assumption is common in recent numerical simulations of combustion instability.[36–38] The study uses methane mass flow rate as the control parameter to investigate the effects of the global equivalence ratio on thermoacoustic instability. In rocket propulsion, both fuel-rich and oxygen-rich combustion modes are possible, which makes the bifurcation behavior under different equivalence ratios the primary focus of this work. Given that the methane mass flow rate is relatively small compared to the total oxidizer mass flow rate, adjusting methane flow has minimal influence on the cold flow characteristics of the engine. Table II summarizes the computational boundary conditions. As the equivalence ratio varies from 1.7 to 0.3, both fuel-rich and oxygen-rich combustion behaviors are encompassed.

The initial conditions involve pre-filling the entire combustion chamber with high-temperature nitrogen gas at 2000 K under a static ambient pressure of 1.4 MPa. This approach facilitates ignition and allows the system to quickly reach the designed operating pressure, thus saving computational resources.

C. Numerical procedure

This study utilizes the open-source CFD software OpenFOAM, specifically a modified version of the reactingFOAM solver,[39] to conduct full-scale three-dimensional detached Eddy simulations (DES). This solver has been widely used in previous large Eddy simulation (LES) and DES studies, particularly for simulating both non-premixed and premixed turbulent combustion.[40,41] The simulations solve the Favre-filtered Navier–Stokes equations for reactive flow, including mass, momentum, species transport, and energy equations. The k–ω SST-based DES turbulence model and the partially stirred reactor (PaSR) model are employed to account for sub-grid scale turbulence and combustion processes in the gas-phase, non-premixed combustion. Since this study focuses on gaseous reactants, gas–liquid interactions are not considered.

The combustion chamber operates at a pressure of 1.3 MPa, which is below the critical pressures of both methane and oxygen. Consequently, the ideal gas law is employed to determine the density of the gas-phase mixture. Consistent with previous studies,[34,42] we assume that the gas-phase mixture behaves ideally, adhering to Fick's law for species diffusion and Fourier's law for heat conduction. Laminar viscosity is calculated using the Sutherland model. For the diffusion coefficients, a Lewis number of unity ($\mathrm{Le} = 1$) is assumed. Additionally, species-specific thermodynamic properties, such as specific heat capacities, are sourced from the JANAF thermochemical tables.

The numerical procedure uses an unstructured mesh, following the Gauss theorem, and relies on the finite volume method (FVM) for spatial discretization. A semi-implicit time integration scheme is employed, with the PIMPLE algorithm (a combination of SIMPLE and PISO) used for pressure–velocity coupling, making it suitable for transient simulations. Diffusion and convection terms are discretized using a second-order central difference scheme, while time integration is performed using the second-order Crank–Nicolson method.[41–43] The physical simulation time for each case is set to 40 ms, ensuring that a sufficient number of acoustic cycles are captured. Referring to previous study,[36] a computational time step of 2×10^{-7} s is employed to accurately resolve turbulent-combustion coupling. Each simulation case requires approximately 16 640 CPU core-hours, with individual CPU cores operating at a frequency of 2.4 GHz.

D. Mesh details and validation

The numerical model employed in this study has been thoroughly validated in our previous research, and readers interested in further details are encouraged to refer to our earlier publication.[21–25,41] Additionally, in the Appendix of this paper, we provide a validation of combustion instability conditions in a single-element model liquid rocket engine burning hydrogen peroxide and methane, where the numerical simulation results are thoroughly compared with experimental measurements.

In this section, we employ three distinct resolution grids to assess the grid independence of a case with an equivalence ratio of 0.8. The size and distribution of these grids have been extensively described in our previous study[25] and are briefly summarized below. The radial distribution of the three meshes is consistent, as the largest mesh size in this direction measures only 1.2 mm and the smallest mesh size is 0.1 mm, thereby ensuring an appropriate spatial resolution in the cross-sectional direction. The grid is clustered near the shear layer to

TABLE II. Boundary conditions.

Part	Boundary condition	Value	Note
Oxidizer inlet	Mass flow rate	5×0.32 kg/s	
	Temperature	1030 K	
	Mass composition	42% O_2 + 58% H_2O	
Fuel inlet	Mass flow rate	$5 \times (0.012 \leq \dot{m} \leq 0.054)$ kg/s	$0.3 \leq \phi \leq 1.7$
	Temperature	300 K	
	Mass composition	100% CH_4	
Walls	No-slip; non-permeable; adiabatic		
Outlet	Wave transmissive	0.8 MPa	Supersonic outlet

ensure accurate calculation of the turbulent mixing of fuel and oxidizer. In the longitudinal direction of the rocket engine, different numbers of grid nodes are used, resulting in maximum grid sizes of 1.2, 1, and 0.6 mm in the combustion chamber, respectively. For the sake of discussion, the three grids are labeled as coarse, medium, and fine, respectively, and the number of hexahedral elements produced by these three meshes is 4.8×10^6, 9.2×10^6, and 13×10^6, respectively.

Figure 2 shows the comparison of acoustic pressure ($p' = p - \overline{p}$) series monitored at Probe 1 (0, 0.056, 0.01 m) with three different grids, and the corresponding FFT results. Temporal data were sampled with an interval of 0–5 ms and a sampling frequency of 500 000 Hz. Monitoring Probe 1 is located at the head of the combustion chamber, close to the wall of the combustion chamber. At the onset of the calculation, all three grids accurately simulate medium-amplitude, periodic pressure oscillations. As time progresses, the amplitude of oscillation gradually increases. In proximity to the wave trough, a smooth waveform is observed instead of a wrinkled one, indicating a transition toward period-1 oscillation and disappearance of higher-order modes. Notably, the coarse grid results exhibit significantly lower oscillation amplitude compared to the other two grids. This discrepancy may stem from limitations imposed by the coarse grid on calculating combustion processes, resulting in inadequate energy transfer from the combustion field to acoustic field. For quantification, FFT analysis provides a comparison of frequencies as well as amplitudes in the acoustic pressure series. We observe that the first peak of the acoustic pressure oscillation occurs around 1399 Hz in all three meshes, while the medium and fine meshes still show consistency around higher-order harmonics, such as 2798 Hz. However, the occurrence of the second mode cannot be captured by the coarse mesh.

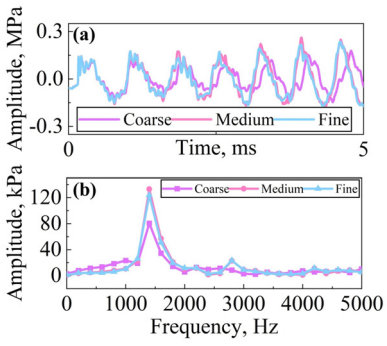

FIG. 2. (a) Temporal evolution of acoustic pressure with different grids monitored at probe 1 and corresponding fast Fourier transform (FFT) results.

To further validate grid independence, we computed the energy-based index M,[44,45] defined as: $M = k_{res}/(k_{res} + k_{sgs})$, where k_{res} represents the resolved turbulent kinetic energy, and k_{sgs} denotes the subgrid-scale turbulent kinetic energy. This index quantifies the contribution of resolved flow structures to the total turbulent kinetic energy, with k_{res} being the component captured by the large Eddy simulation (LES) model and k_{sgs} the component modeled by the subgrid-scale model. The simulation is deemed grid-independent and, thus, valid when the energy index M exceeds 85%.[46] Figure 3 presents the contour lines of the index M calculated using a medium grid resolution. We observe that M exceeds 0.85 across nearly all regions, except for a few areas near the walls. This exception arises from the application of the $k-\omega$ SST model in the near-wall regions. However, since the focus of this study is on the core turbulent areas, such as the vicinity of shear layers, the medium grid resolution sufficiently meets the computational requirements of this research. Therefore, considering a compromise between computational accuracy and efficiency, the medium mesh is employed for subsequent parametric analysis.

IV. RESULTS AND DISCUSSION

A. Mode switching in LREs

In this section, we investigate the multi-bifurcation process that arises in the system dynamics of a rocket burner as the methane mass flow rate is continuously reduced. We observe that the mode switching occurs through quasiperiodic oscillations, specifically from a period-1 oscillation (1L mode) to a quasiperiodic state and then to another period-1 oscillation (2T mode). In more detail, when operating the burner at a global equivalence ratio ranging from 1.7 to 0.5, thermoacoustic system dynamics are predominantly characterized by period-1 oscillation (1L). However, within a global equivalence ratio of 0.3,

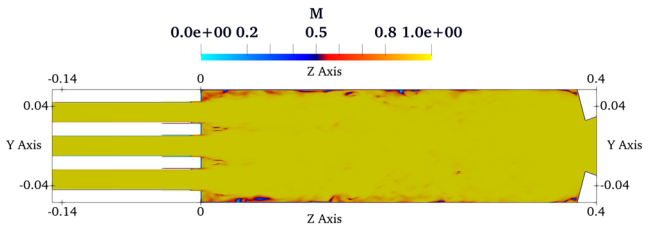

FIG. 3. Contour of the index M in the y–z plane with medium mesh.

although still dominated by period-1 oscillation, there is an observed shift in the oscillation mode (2T). Furthermore, at an equivalent ratio of 0.4, we observe the coexistence of three periods in a quasi-periodic state. Detailed evidence supporting these findings is presented below.

Figure 4 depicts the results of the system dynamics monitored at Probe 2 (0, 0.056, 0.38). The data points in the time series were sampled at a frequency of 500 kHz, corresponding to a sampling interval of 2 μs. As demonstrated in Fig. 4(a) by the FFT results, when the equivalent ratio is 1.7, the spectrum indicates that a single frequency at 1500 Hz completely dominates the system's oscillations. When the global equivalence ratio decreases from 1.7 to 0.5, we observe the following: (1) isolated peaks in the FFT results are concentrated around 1500 Hz, while other frequencies approximate noise levels; and (2) the amplitude of pressure oscillations decreases from 238 kPa ($\phi = 1.7$) to 71 kPa ($\phi = 0.5$). These phenomena indicate that within the range of $0.5 \leq \phi \leq 1.7$, the system dynamics are dominated by period-1 oscillations, with a tendency for the oscillation amplitudes to decrease. Intriguingly, at a global equivalence ratio of 0.3, another single frequency at 10 098 Hz entirely dominates the spectrum distribution, a phenomenon referred to as mode switching in dynamical systems theory. Furthermore, when the global equivalence ratio is reduced to 0.4, three frequencies coexist in the spectrum—specifically at 1440, 3999, and 9438 Hz, respectively—suggesting potential quasi-periodic oscillation resulting from interactions between these pressure oscillations corresponding to different modes (not commensurate). Such a phenomenon indicates that the thermoacoustic system has evolved into a quasi-periodic state with three-periods,[16,47] which is still unique and has not been reported in the field of rocket propulsion. To facilitate further analysis of typical dynamical regimes, Figs. 4(b)–4(d) present the time series and (b1)–(d1) magnified waveforms. Based on the time series, it is observed that constant amplitude and periodic oscillations occur at a global equivalence ratio of 1.7. However, at a global equivalence ratio of 0.4, interaction between multiple modes including acoustic and non-acoustic modes results in loss of periodicity in the time series. When $\emptyset = 0.3$, the time series exhibits a distinct "beat" phenomenon, indicating the presence of two resonant motions within the system characterized by a small frequency difference. The combination of these resonant motions with smaller difference results in periodically and gradually fluctuating amplitudes. Figures 4(b2)–4(d2) depict the results of phase space reconstruction in the corresponding dynamical states. The method of phase space reconstruction plays a crucial role in comprehending the latent nonlinear characteristics within time series data and can further complement the findings overlooked in linear analysis. A detailed mathematical explanation of the phase space reconstruction method is available in a previously published paper by Guan *et al.*[47] For $\emptyset = 1.7$, the phase diagram exhibits a fully open loop structure. In contrast, at $\emptyset = 0.3$, the phase trajectory of beat motion invades from an outer loop structure to an inner one, forming a "doughnut-like" loop. Finally, at $\emptyset = 0.4$, interaction between three incommensurate frequencies causes further inward invasion of pressure's phase trajectory on the diagram, resulting in non-closure of its trajectory. Previous studies by Pawar *et al.*[48] and Liu *et al.*[21] have demonstrated that increasing the preheated reactant temperature preserves the bifurcation routes of system dynamics within the global equivalence ratio parameter space, although the bifurcation points occur earlier. These studies indicate that investigating system dynamics bifurcations within the global equivalence ratio parameter space holds general significance.

Figure 5 presents the time series, short-time Fourier transform results, and recurrence plot results for the three distinct dynamical states. In the short-time Fourier transform [Figs. 5(a1), 5(b1), and 5(c1)], it is observed that for $\emptyset = 1.7$, a prominent white line consistently appears near the 1500 Hz throughout the computation time, indicating the system dynamics are predominantly governed by a single frequency from start to finish. For $\emptyset = 0.4$, oscillation around 1400 Hz dominates during the initial time interval of 0–6 ms; however, as time progresses, the amplitude gradually diminishes and three distinct dark red bands coexist simultaneously. For $\emptyset = 0.3$, at initial instants from 0 to 8 ms, the system is dominated by 1500 Hz, which, as time evolves, gives way to oscillations around 10 kHz. At this time, the bright red bands were observed near 10 kHz, while dark red bands were also observed near 12 kHz, respectively. This discussion effectively addresses limitations in previous FFT results in time-history analysis. Recurrence plots (RP) are introduced in this section as an

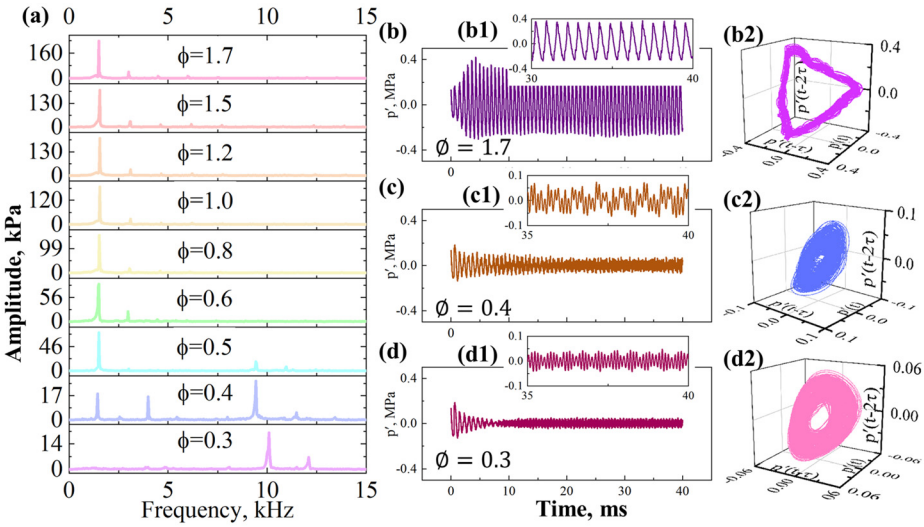

FIG. 4. Overview of system dynamics under the parameter space of equivalence ratio ($1.7 \leq \phi \leq 0.3$): (a) FFT results of the acoustic pressure (p'); (b)–(d) Time traces, (b1)–(d1) wave form, and (b2)–(d2) phase portraits for three different dynamical states.

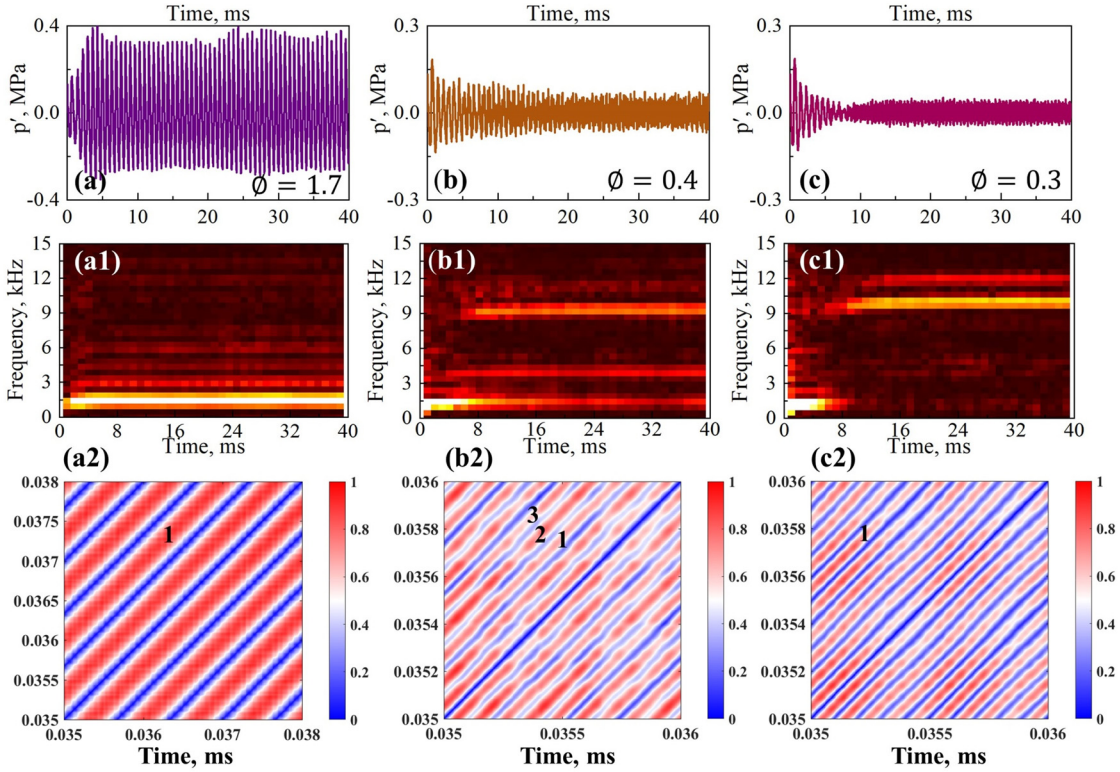

FIG. 5. Time series, short time Fourier transform (STFT) results, and recurrence plots (RP) for the various dynamical states: (a) Ø = 1.7, (b) Ø = 0.4, and (c) Ø = 0.3.

effective graphical method to identify different nonlinear states of thermo-acoustic systems. The application of RP helps researchers distinguish the repetitive patterns and structural features in time series data. The fundamental concept of RPs is to monitor the temporal progression of high-dimensional phase-space trajectories and identify their recurrent points. Various nonlinear states can be distinguished by distinct geometric patterns. For instance, periodic states are indicated by diagonally-aligned recurrent structures in a RP. A more comprehensive mathematical description was provided in the earlier work by Eckmann *et al.*[49] and Guan *et al.*[50] Figures 5(a2), 5(b2), and 5(c2) illustrate the results of the RPs for the three equivalence ratios. In recurrence plots (RPs), it is well established that various periodic states can be identified by quantifying the off-colored diagonal bands located between two full-blue diagonal bands corresponding to $S \approx 0$, which represent a complete cycle. For Ø = 1.7, the RP exhibits a distinct red and blue striped structure, indicative of the presence of a complete period-1 limit cycle state. For Ø = 0.4, a more complex periodic structure is observed for a time interval of 1 ms. First, the lightening of the red band as well as the irregular boundaries represent a reduction in the distance between different points on the phase trajectory. Second, as depicted in Fig. 5(b2), there exist three lighter red bands (labeled 1, 2, and 3) between the two darker blue bands, indicating the presence of three distinct periods of oscillation. For Ø = 0.3, an alternating distribution between lighter red and blue bands is observed, signifying a reduced separation between different points on the phase trajectory while still maintaining a period-1 oscillation. Upon closer examination along the diagonal from bottom left to top right, it becomes apparent that the red band exhibits uneven distribution with intermittent decreases in S value (resulting in thickening of the blue band). These phenomena suggest that amplitude changes occur due to beat motion.

In this study, we employed the three-dimensional acoustic software COMSOL Multiphysics to perform a theoretical analysis of the combustion chamber's acoustic characteristics. This analysis aids in understanding the different acoustic frequencies and their corresponding modes. It is assumed that the combustion chamber is filled with high-temperature gas at a uniform temperature of 3000 K. Table III lists several theoretical solutions of acoustic characteristic frequencies and their corresponding modes that are close to the frequencies of interest in this study. Under these conditions, we identified 1441 Hz as the theoretical 1L acoustic frequency and 9366 Hz as the theoretical 2T acoustic frequency. Referring to the DES results obtained at a global equivalence ratio of 0.4, three unstable frequencies were observed: 1440, 3999, and 9438 Hz. The 1440 Hz frequency corresponds to the 1L acoustic frequency, while the 3999 Hz frequency is identified as a

TABLE III. Theoretical analysis of acoustic frequency in the combustion chamber.

Acoustic modes	1L	2L	3L	2T	1R
Frequency	1441	2882 Hz	4323 Hz	9366 Hz	11 753 Hz

non-acoustic frequency since it lies between the theoretical 2L and 3L acoustic frequencies. Additionally, the DES result of 9366 Hz closely matches the theoretical 2T acoustic frequency of 9438 Hz. The DES result is slightly lower than the theoretical calculated value and can be attributed to the non-uniform temperature distribution in the cross section direction. In support of the previous theoretical analysis, Fig. 6 presents instantaneous snapshots of pressure at three interested moments for two global equivalence ratio conditions. The two-dimensional slice of Fig. 6(a) was defined at $x = 0$ cm, encompassing a range of $-1.5\,\text{cm} \le z \le 40\,\text{cm}$ and $-5.7\,\text{cm} \le y \le 5.7\,\text{cm}$. The two-dimensional slice of Fig. 6(b) was defined at z = 1 cm, encompassing a range of $-5.7\,\text{cm} \le \text{x}, y \le 5.7\,\text{cm}$. For Ø = 1.7, the high-pressure wave initially emerges at the combustion chamber's head at 35.30 ms. Subsequently, it propagates downstream through the combustion chamber until reaching the vicinity of the nozzle by 35.55 ms. Due to higher flow velocity in the nozzle's expansion section exceeding one Mach, a rigid acoustic boundary forms, reflecting back the pressure wave toward the combustion chamber. The pressure wave then continues its upward propagation against the average flow direction, ultimately returning to reach the head of the combustion chamber at 35.95 ms, completing an acoustic propagation cycle dominated by 1L acoustic mode. For Ø = 0.3, the acoustic propagation process occurs in the cross-sectional direction of the combustion chamber. At 37.45 ms, two high-pressure waves (left and right) were observed propagating clockwise (or counterclockwise) within the cross section. Over time, these pressure waves exhibit rotational motion in a transverse direction. By 37.50 ms, two waves (top and bottom) are reached across the cross section before repeating this pattern cyclically. Consequently, it can be inferred that the 2T mode dominates the propagation of acoustic waves.

B. Synchronization between pressure and combustion fields

The synchronous coupling of acoustic pressure and combustion fields is an important physical mechanism driving combustion instability. Figure 7 illustrates the instantaneous isosurface of the temperature (T = 2000 K) in the combustion chamber and is colored with the magnitude of the velocity to provide further insight into the combustion flow field. In this paper, the isosurfaces (T = 2000 K) are used to identify the flame position.[28,33,51] As shown in Fig. 7, the flame length in the fuel-rich condition is significantly shorter than that in the oxidizer-rich condition. The injection method adopted in this paper is gaseous oxidizer as the injector center and gaseous fuel around. In fuel-rich conditions, the oxidizer in the center is consumed more quickly, resulting in a more compact flame at the front of the combustion chamber. For the 1L mode, the front of the combustion chamber is the anti-node of the mode shape. When the flame is concentrated here, it is more beneficial for the acoustic field to obtain energy from the combustion field and then amplify the acoustic oscillations in the longitudinal direction. As the mass flow rate of fuel decreases further, a corresponding reduction in the global equivalence ratio is achieved. Under oxidizer-rich conditions, the turbulent flame undergoes significant elongation, resulting in enhanced longitudinal uniformity. In the cross section direction, the 2T mode is activated by the flames downstream of the surrounding four injectors (positioned at the top, bottom, left, and right). The intricate competition and cooperation among multiple acoustic modes lead to the emergence of quasi-periodic oscillation.

To quantitatively track the time evolution of acoustic pressure and the combustion field, monitoring points were placed near the initial shear layer downstream of each of the five injectors. The coordinates of these monitoring points are as follows: probe 3 (0, 0.0115, 0.01) for injector 1; probe 4 (0, 0.0455, 0.01) for injector 2; probe 5 (−0.0455, 0, 0.01) for injector 3; probe 6 (0, −0.0455, 0.01) for injector 4; and probe 7 (0.0455, 0, 0.01) for injector 5. Figure 8 presents an overview of the synchronization dynamics of the acoustic pressure (p') and the temperature perturbation (T′). For the time series, we observe a strong coupling between p' and T′ when Ø = 1.7, that is, the two

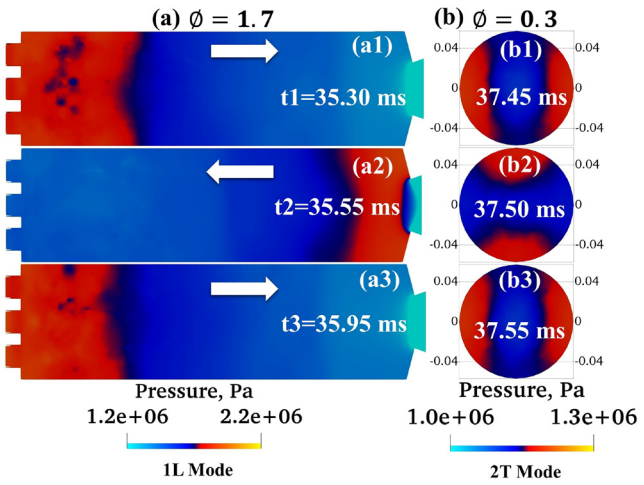

FIG. 6. Three instantaneous snapshots of the pressure in the cycle analysis: (a) Ø = 1.7 and (b) Ø = 0.3.

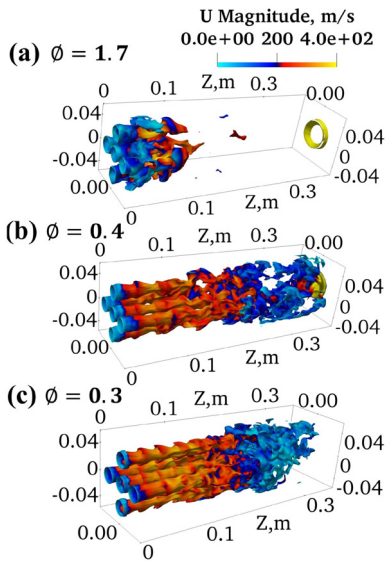

FIG. 7. Comparison of instantaneous isosurface of temperature at T = 2000 K colored by the magnitude of velocity: (a) Ø = 1.7, (b) Ø = 0.4, and (c) Ø = 0.3.

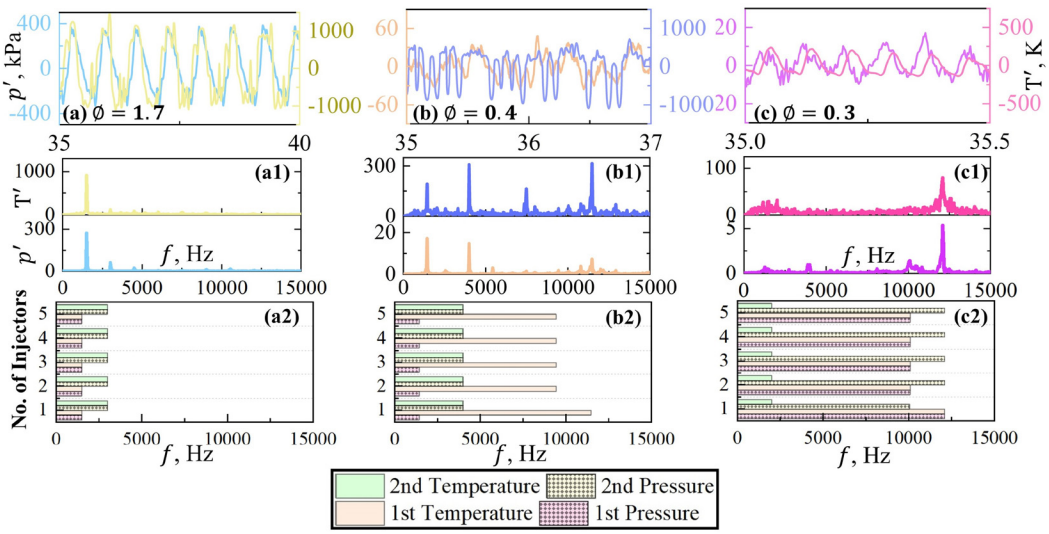

FIG. 8. Overview of the synchronization dynamics of acoustic pressure and temperature near the shear layer downstream of the five injectors: (a)–(c) time series monitored at Probe 3, (a1)–(c1) corresponding FFT results and (a2)–(c2) the first two order dominant frequencies.

harmonic signals share the same oscillation frequency and almost zero phase difference. For $Ø = 0.3$, we observe a clear phase difference, but the oscillation frequency is still the same; However, for $Ø = 0.4$, the time series of both p' and T′ are obviously non-harmonic. As a quantitative comparison of the time series, the FFT method is employed to analyze the frequency spectrum of the signals. As shown in Figs. 8(a1) and 8(c1), at $Ø = 1.7$, the dominant frequency of both the pressure and temperature signals downstream of injector 1 is fully locked to the 1L mode. At $Ø = 0.3$, the dominant frequency of the pressure and temperature signals downstream of injector 1 is fully locked to the 2T mode. However, at $Ø = 0.4$, the frequency spectrum of the pressure and temperature signals downstream of injector 1 exhibits a more complex, non-locked relationship. At this point, the first two dominant frequencies of the temperature oscillations are 11 477 and 3999 Hz. Meanwhile, the first two dominant frequencies of the acoustic pressure oscillations are 1440 and 3999 Hz. Additionally, we observed that the pressure oscillation spectrum downstream of Injector 1 exhibits a lower peak near the 2T acoustic frequency. This is attributed to the sampling point being located near the center of the cross section and close to the node of the 2T acoustic mode, which results in a significant suppression of transverse oscillations. To comprehensively compare the frequency-locking of pressure (p') and temperature (T′) downstream of different injectors, we extracted the dominant frequencies of these two signals in the first two orders, as shown in Figs. 8(a2)–8(c2). As illustrated in Fig. 8(a2), both the first dominant frequency and its higher-order harmonics show complete frequency-locking in p' and T′ downstream of different injectors. In contrast, Fig. 8(c2) shows that only the first dominant frequency (2T mode) exhibits strong locking across the injectors, while its higher-order harmonics do not. As shown in Fig. 8(b2), for $Ø = 0.4$, the first dominant frequency of the p' and T′ signals downstream of the five injectors corresponds to the 1L acoustic frequency and the 2T acoustic frequency, with the second dominant frequency consistently at 4000 Hz. The authors would like to further point out that the origin of the 4000 Hz oscillation remains unclear; prior knowledge suggests that it is not an acoustic frequency.

Figure 9 presents an overview of the synchronous dynamics between pressure and methane mass fraction. The coupling between pressure (p') and methane (CH4′) shows a certain similarity to the coupling between pressure (p') and temperature (T′), and therefore, a brief description is provided below. For $Ø = 1.7$, according to the results in Fig. 9(a), the most notable difference is the presence of a phase lag between the acoustic pressure and the methane mass fraction, with the change in methane mass fraction occurring earlier than the changes in both pressure and temperature. This is an intriguing finding, indicating the existence of a distinct characteristic time in the combustion process. The pressure response to temperature changes is immediate, while it lags behind the variations in methane mass fraction. For $Ø = 0.4$, a notable distinction is that the spectrum of the methane mass fraction signal exhibits a significantly low amplitude in the transverse modes ($f > 5000$ Hz). In the first two dominant frequencies of the methane mass fraction signal, only the 1L mode frequency and oscillations around 4000 Hz were clearly observed, with no transverse acoustic frequencies detected. For $Ø = 0.3$, although the time series of both the pressure and methane mass fraction exhibit simple harmonic oscillations, a relatively large phase difference between them (with methane changes occurring earlier than the pressure response) may lead to weak coupling between the acoustic pressure oscillations and the combustion field.

C. Spatio-temporal analysis of mixing dynamics

In this section, we present a comprehensive investigation of mixing dynamics under two distinct dynamical states, $Ø = 1.7$ and $Ø = 0.3$. Our objective is to elucidate the mixing dynamics using the mixture fraction[21] under both fuel-rich and oxidizer-rich conditions. This analysis aims to provide a deeper understanding of the physical mechanisms driving mode switching in these regimes.

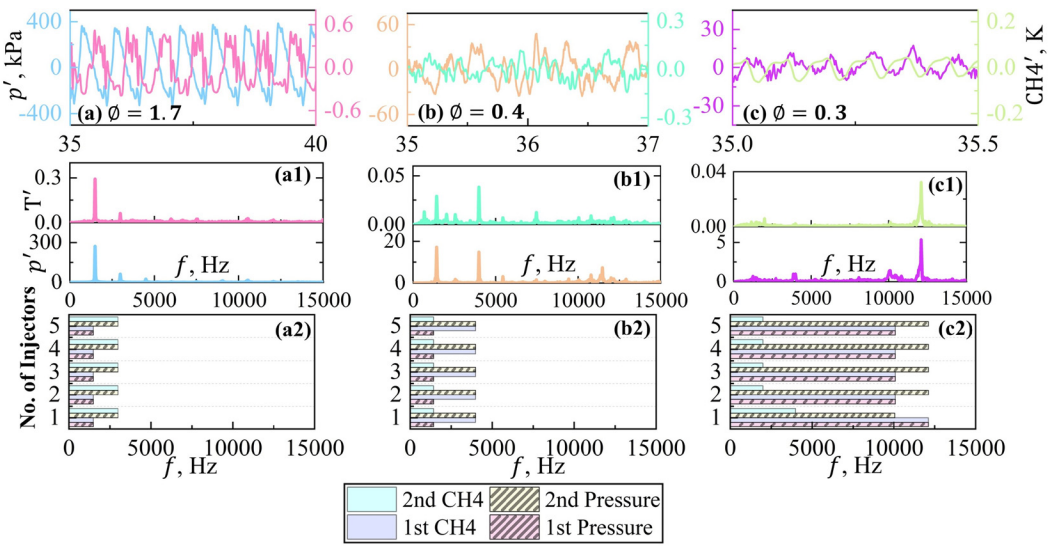

FIG. 9. Overview of the synchronization dynamics of acoustic pressure (p') and mass fraction of methane ($CH4'$) near the shear layer downstream of the five injectors: (a)–(c) time series monitored at probe 3, (a1)–(c1) corresponding FFT results, and (a2)–(c2) the first two order dominant frequencies.

Figure 10 illustrates the unsteady behavior of the mixture fraction field at the moment of interest for Ø = 1.7 and Ø = 0.3. The two-dimensional slice in Fig. 10 was defined at $x = 0$ cm, encompassing a range of $-1.5\,\text{cm} \le z \le 15\,\text{cm}$ and $-5.7\,\text{cm} \le y \le 5.7$ cm. The mixture fraction is a dimensionless parameter that quantifies the mixing of fuel and oxidizer. A mixture fraction value of +1 indicates complete fuel flow, while a value of 0 represents pure oxidizer flow. Detailed mathematical expressions can be referred to our previous papers.[24] The value of stoichiometric mixture fraction is 0.095, represented by white isocontour lines. As shown in Figs. 10(a1) and 10(a2), at time t = 0, the high-pressure wave propagates near the dump plane, significantly shortening the penetration length of the stoichiometric mixture fraction and resulting in a more compact flame. At t = T/2, the high-pressure wave moves away from the dump plane, significantly lengthening the penetration length of the stoichiometric mixture fraction, resulting in a longer flame. The mixture fraction exhibits a significant disparity for Ø = 0.3, with lower values observed throughout the combustion chamber compared to the fuel-rich condition. We also observed that under fuel-rich conditions, the distribution of the mixture fraction becomes more continuous with fewer interruptions. In Fig. 10(a3), we observe significant differences as the axial coordinate range from 10 to 20 cm. Compared to Fig. 10(a1), the pure mixing process of fuel and oxidizer has disappeared, and instead, local oxygen-rich combustion and intense combustion near the stoichiometric ratio have taken place.

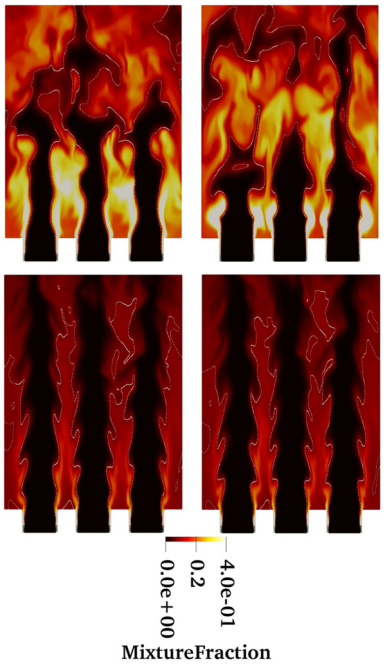

FIG. 10. Instantaneous contours of the mixture fractions on the y-plane: (a1, top left) Ø = 1.7, t = 0; (a2, top right) Ø = 1.7, t = T/2; (b1, bottom left) Ø = 0.3, t = 0; and (b2, bottom right) Ø = 0.3, t = T/2.

Figure 11 presents scatter plots of temperature vs mixture fraction at two different time instants. The color of the scatter points in the figure represents different axial positions. The number of scatter points in each image exceeded 1×10^6, representing the central node of each grid cell in the region of interest. As shown in Fig. 11(a1), Near the dump plane (z = 0 cm), fuel preheating dominates, with the temperature mostly in the range of 300–1030 K. As the flow progresses downstream, fuel-rich combustion occurs (denoted by the orange scatter points), but the local mixture fraction is significantly higher than the stoichiometric ratio ($0.5 \le$ mixture fraction ≤ 1.0), resulting in lower temperatures (primarily 300–1500 K). Further downstream, the local mixture fraction approaches the stoichiometric ratio (yellow points), causing the combustion temperature to rise. At the green points (representing a further axial position), a mixture fraction between 0 and

0.4 suggests that various stages of combustion occur simultaneously: fuel-rich, oxidizer-rich, and stoichiometric combustion. In the slightly blue region, as the fuel diminishes and the oxidizer increases, oxidizer-rich combustion dominates. Closer to z = 10 cm, the fuel–oxidizer ratio reaches stoichiometric conditions (blue points), resulting in the highest combustion temperatures and more intense chemical reactions. As shown in Fig. 11(a2), when the high-pressure wave moves away from the dump plane, the overall geometric shape of the scatter-plot is similar to that at time T1. However, the spatial position of the heat release region shifts downstream. Near z = 10 cm (blue scatter points), the mixture is predominantly oxidizer-rich, as opposed to being at the stoichiometric ratio at time T1, which is evidenced by the changing spatial distribution of temperatures and mixture fractions in this region. In Fig. 11(a3), we observe significant differences as the axial coordinate range shifts from 10 to 20 cm. Compared to Fig. 11(a1), the pure mixing process of fuel and oxidizer has disappeared, and instead, local oxygen-rich combustion and intense combustion near the stoichiometric ratio have taken place. The temperature ranges from 1500 to 2800 K, as depicted in Fig. 11(a4), while the mixture fraction varies between 0.018 and 0.34, indicating the prevalence of combustion near the stoichiometric ratio and localized oxygen-rich combustion at this stage. This observation implies that with gradual fuel depletion, there is an escalation in combustion intensity, leading to a significant elevation in temperature. As shown in Figs. 11(b1) and 11(b2), at different time instants, when transverse combustion instability dominated by the 2T acoustic mode is activated, no significant differences are observed in the axial distribution of the mixing dynamics. In Fig. 11(b1), we observe distinct mixing dynamics, localized oxygen-rich combustion, and fuel-rich combustion. Interestingly, however, under extremely fuel-rich conditions (mixture fraction > 0.5), no significant combustion was observed. This lack of combustion in areas of high fuel abundance near the dump plane suggests that inadequate mixing inhibits effective combustion. In Figs. 11(b3) and 11(b4), Within the axial range from 10 to 20 cm, a relatively narrow mixture fraction range from 0 to 0.1 is observed, indicating the presence of only oxygen-rich combustion and combustion near the stoichiometric ratio.

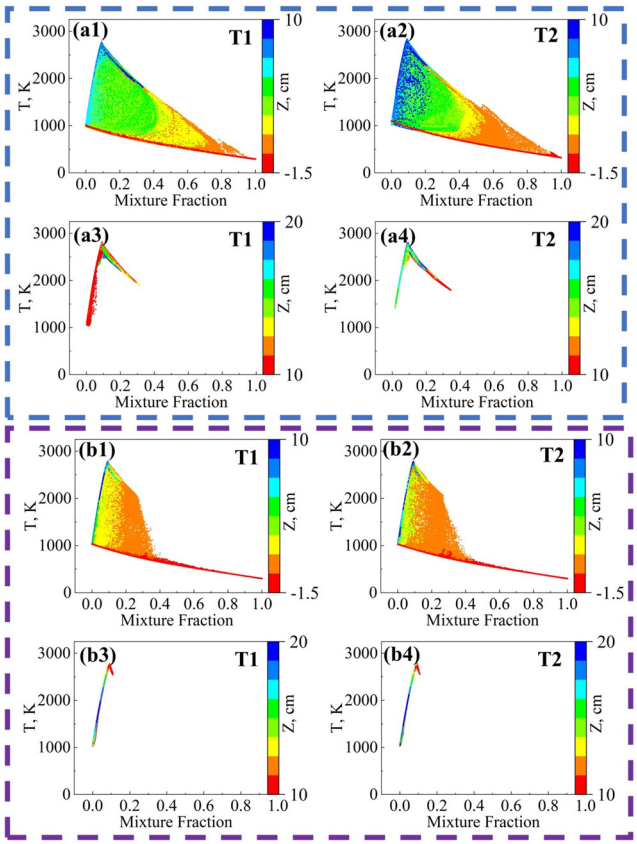

FIG. 11. Scatter plots of the temperature under the space of the mixture fraction. The rainbow color map represents the distance of the scatter from the dump plane. (a1)–(a4) Ø = 1.7 and (b1)–(b4) Ø = 0.3. T1 and T2 represent two different instants in time, corresponding to those in Fig. 10. The scatterplot in the first column samples within the range of −1.5 cm ≤ z ≤ 10 cm, while the second column samples within the range of 10 cm ≤ z ≤ 20 cm.

D. Spatio-temporal analysis of flame dynamics

To further analyze flame dynamics, this section introduces the dimensionless flame index (FI), with its mathematical expression detailed in prior studies.[52] The FI is used to differentiate between premixed flames and diffusion flames during engine operation. By definition, the Flame Index can assume only three values: +1 for premixed flames, −1 for diffusion flames, and 0 where no combustion occurs. To eliminate the possibility of pseudo-flame structures, following

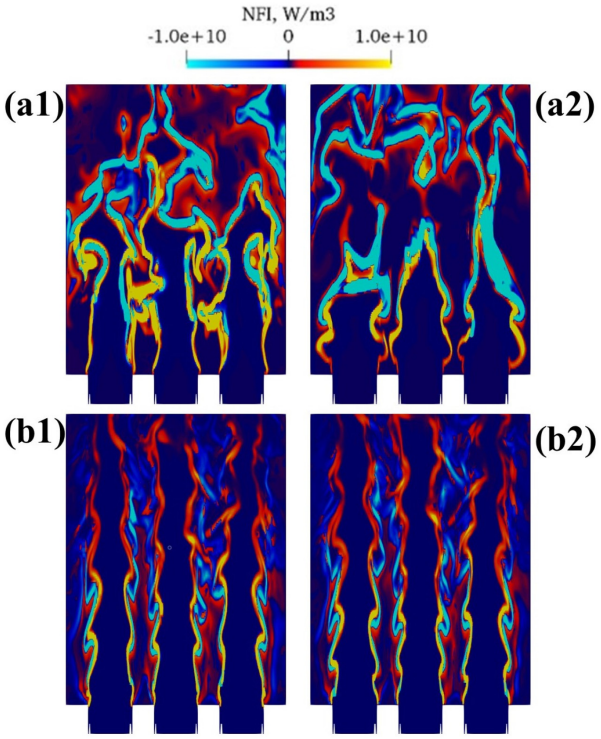

FIG. 12. Instantaneous contours of the NFI on the y-plane: (a1) Ø = 1.7, t = 0; (a2) Ø = 1.7, t = T/2; (b1) Ø = 0.3, t = 0; and (b2) Ø = 0.3, t = T/2.

Nguyen and Sirignano,[51] we combine the flame index with the heat release rate (HRR), leading to a modified mathematical expression: NFI = FI × HRR. For this expression, NFI > 0 indicates a premixed flame, NFI < 0 represents a diffusion flame, and NFI = 0 signifies the absence of a flame. Figure 12 illustrates the unsteady behavior of the flame dynamics using NFI at the moment of interest for (a1, a2) Ø = 1.7 and (b1, b2) Ø = 0.3. The time instants and regions selected in the figure correspond to those in Fig. 10. As shown in Fig. 12(a1), at this moment, the pressure wave reaches the vicinity of the dump plane, causing the flame front to distort due to the baroclinic torque,[28] resulting in a sudden increase in heat release. More specifically, premixed combustion (NFI > 0) occurs near the dump plane, while further downstream, diffusion flames (NFI < 0) begin to emerge. The flame fronts downstream of the different jets overlap each other, representing the strong coupling between the different injector jets. As the pressure wave moves away [as shown in Fig. 12(a2)], the different flame fronts downstream of the dump plane begin to separate, and weaker coupling between the injectors is observed. At the same time, the flame fronts become more continuous, with reduced distortion, indicating a decrease in heat release. We also qualitatively observed an increase in diffusion flames compared to the previous time instant. At Ø = 0.3, as shown in Figs. 12(b1) and 12(b2), the flame front appears continuous, and the weakest coupling between injectors is observed. Additionally, along the engine axis, no significant differences in the spatial distribution of premixed and diffusion flames are detected.

To quantitatively analyze the combustion modes at different axial positions and time instants, Fig. 13 presents the percentage of total heat release corresponding to each combustion mode. This allows for a clearer understanding of the contribution of premixed and diffusion flame. The different regions and time instants shown in the figure correspond to those in Fig. 10. As shown in Figs. 13(a1)–13(a4), in region 1 ($-1.5\,\text{cm} \le z \le 10\,\text{cm}$), due to the influence of the high-pressure wave, the ratio of premixed flames to diffusion flames at time T1 is approximately 3:2. As the high-pressure wave moves away, the proportion of diffusion flames slightly increases from 39.7% to 43.6%. A more significant difference is observed in region 2, where, in the range of $10\,\text{cm} \le z \le 20\,\text{cm}$, diffusion flames dominate the entire combustion process. The distinctly different combustion modes in regions 1 and 2 provide evidence for the presence of the 1L mode. As shown in Figs. 13(b1)–13(b4), when ϕ=0.3, premixed flames continue to dominate the combustion in region 1 at both T1 and T2. However, in region 2, a notable difference emerges compared to ϕ=1.7: premixed flames still dominate, although the proportion of diffusion flames has slightly increased relative to region 1. In thermoacoustic instability dominated by the 2T mode, no qualitative differences in combustion modes are observed with changes in spatial position. In contrast, the thermoacoustic instability dominated by the 1L mode behaves differently, providing quantitative evidence for the mode transition phenomenon discussed in this study. This suggests that the spatial variation in combustion modes is a key mechanism driving mode transitions in thermoacoustic instability.

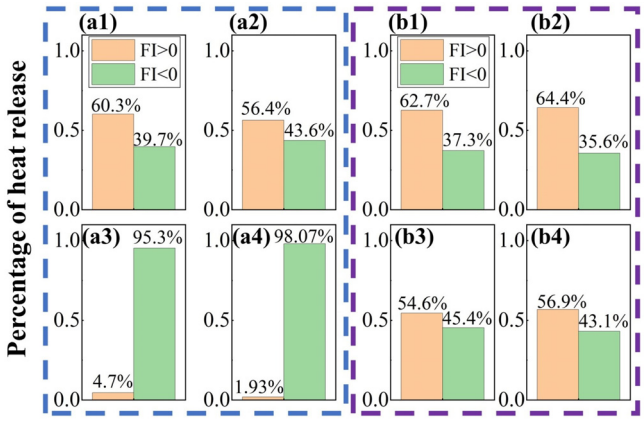

FIG. 13. Percentage of total heat release in the different combustion modes: (a1)–(a4) Ø = 1.7, (a1) t = T1, region 1, (a2) t = T2, region 1, (a3) t = T1, region 2, (a4) t = T2, region 2; (b1)–(b4) Ø = 0.3, (b1) t = T1, region 1, (b2) t = T2, region 1, (b3) t = T1, region 2, and (b4) t = T2, region 2.

V. CONCLUSIONS

In this study, three-dimensional detached Eddy simulation (DES) with a global multi-step chemical reaction kinetics mechanism have been performed to numerically investigate combustion instability in a multi-element model liquid rocket engine burning hydrogen peroxide and methane. Specifically, we focused on the thermo-acoustic system's dynamical bifurcation process under the parameter space of global equivalence ratio ($0.3 \le \phi \le 1.7$) and the spatiotemporal evolution of the combustion flow field under various dynamical states. The main conclusions are as follows:

1. Multi-bifurcation and mode switching: As the methane mass flow rate decreases, the thermoacoustic system undergoes a multi-bifurcation process with notable mode switching. At an equivalence ratio of $\phi = 1.7$, the system exhibits period-1 oscillations dominated by the longitudinal acoustic mode (1L) with a frequency around 1500 Hz. A decrease in the global equivalence ratio to $\phi = 0.3$ shifts the thermoacoustic system to the second-order acoustic mode (2T) with a dominant frequency near 10 098 Hz. At $\phi = 0.4$, the system transitions to a quasi-periodic state with three coexisting frequencies (1440, 3999, and 9438 Hz), indicating complex interactions between acoustic (1L, 2T) and non-acoustic modes. This transition highlights how variations in the equivalence ratio impact mode switching and the emergence of multi-frequency dynamics. Recurrence plot analysis reveals distinct periodic and quasi-periodic structures, confirming the nonlinear behavior during bifurcation.
2. Coupling between acoustic pressure and combustion fields: The coupling between acoustic pressure and the combustion field is crucial in driving TAI and mode switching. At fuel-rich conditions ($\phi = 1.7$), a compact flame forms near the acoustic antinode of the 1L mode. As the equivalence ratio decreases, the flame extends axially, transitioning the system from the 1L to the 2T mode. At $\phi = 1.7$ and $\phi = 0.3$, the acoustic pressure is frequency-locked with combustion fields like temperature and methane mass fraction. However, at $\phi = 0.4$, this frequency-locking is lost, leading to quasi-periodic oscillations. Specifically, at $\phi = 1.7$, large, periodic oscillations cause zero phase difference between pressure and temperature, while a phase lag between pressure and methane mass fraction indicates a combustion delay, with methane oscillations preceding changes in temperature and pressure.

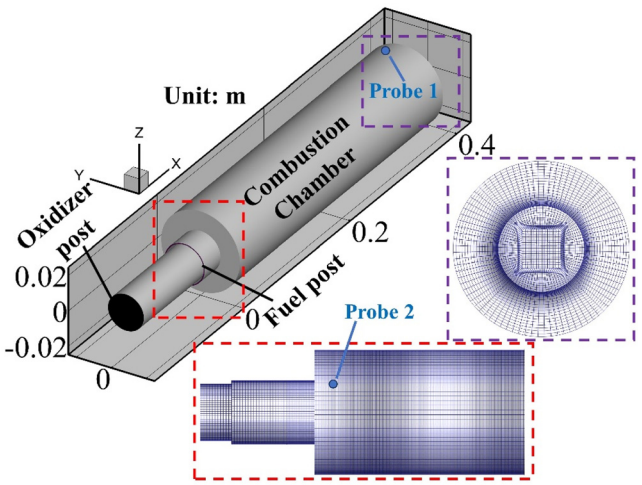

FIG. 14. The geometric configuration of the single-element model rocket engine, along with the corresponding schematic of the local structured mesh, which is identical to that used in our recent studies.[25]

3. Mixing dynamics: The mixing dynamics play a role in driving mode switching. Under fuel-rich ($\phi = 1.7$) conditions, the penetration length of the stoichiometric mixture fraction line is shorter compared to oxidizer-rich ($\phi = 0.3$) conditions, leading to a more compact combustion region. Fuel preheating is observed near the dump plane in the axial direction, followed by local fuel-rich combustion, oxidizer-rich combustion, and stoichiometric combustion downstream. As the global equivalence ratio decreases, the spatial distribution of the mixture fraction field changes, particularly reducing local fuel-rich combustion. Nonetheless, regions of local fuel-rich and high oxidizer concentrations persist along the flow direction, following previously observed combustion patterns.
4. Flame dynamics: The spatial variation in combustion modes is a critical factor driving mode switching in thermoacoustic instability (TAI). At $\phi = 1.7$, combustion in region 1 ($-1.5\,\text{cm} \le z \le 10\,\text{cm}$) is predominantly characterized by premixed flames, while diffusion flames dominate the dynamics in the downstream region 2 ($10\,\text{cm} \le z \le 20\,\text{cm}$). At $\phi = 0.3$, region 1 remains dominated by premixed flames, and no qualitative change is observed in region 2, where premixed flames continue to prevail. These findings underscore the importance of spatial variations in combustion modes in influencing thermoacoustic behavior.

APPENDIX: VERIFICATION OF NUMERICAL METHODOLOGY

In this section, the effectiveness of the numerical algorithm is validated through comparison with experimental measurements. We simulate a model liquid rocket engine known as the continuously variable resonant chamber (CVRC), designed by Purdue University. The CVRC features a single coaxial injector element for hydrogen peroxide/methane combustion and is capable of exhibiting thermoacoustic instability. The geometric dimensions of the coaxial injector are identical to those used in the multi-element engine described earlier, with the combustion chamber diameter corresponding to the single flow tube area of the multi-element engine used in this paper. This experimental setup allows for continuous variation of the oxidizer post length, facilitating the study of acoustic resonance effects on self-excited longitudinal combustion instability. Experimental results[53] indicate that as the oxidizer post length is varied continuously, the thermoacoustic system transitions from stable ($\text{Lox} = 9\,\text{cm}$) to unstable ($12\,\text{cm} \le \text{Lox} \le 14\,\text{cm}$). This study uses experimental measurements from the engine configuration with an oxidizer post length of 14 cm to validate the numerical model. Related work has been discussed extensively in our recent publications, so we would not elaborate further here. Interested readers can refer to our previous papers for more details.[21–23,25] Figure 14 shows the three-dimensional geometric configuration of the CVRC and the corresponding schematic of the local structured mesh. The validation case presented in this section utilizes a hexahedral structured mesh comprising 2.48×10^6 hexahedral cells. The combustion chamber has a length of 38.1 cm, with the oxidizer post length fixed at 14 cm, and a chamber diameter of 4.5 cm. During the experiments, a high-frequency pressure sensor was installed on the chamber wall, 37 cm downstream from the dump plane ($x = 0\,\text{cm}$), to monitor pressure variations over time. Accordingly, a monitoring point is placed at Probe A1 (37, 0, 2.2 cm) for quantitative comparison between numerical simulation results and experimental measurements. Additionally, probe 1 is positioned at the end of the combustion chamber wall and corresponds to the pressure antinode of the first acoustic mode (1L).

Figure 15 displays the time series of pressure and the corresponding FFT results. As shown, periodic and high-amplitude acoustic oscillations occur within the combustion chamber, consistent with experimental measurements. The FFT analysis reveals that the pressure signal's spectrum is dominated by a single frequency, with higher-order harmonics also present. Table IV compares the first three dominant frequencies and their corresponding peak-to-peak amplitudes with experimental measurements. Note that the peak-to-peak amplitude represents the value obtained by subtracting the trough from the peak. As shown in the table, the error in the dominant frequency is

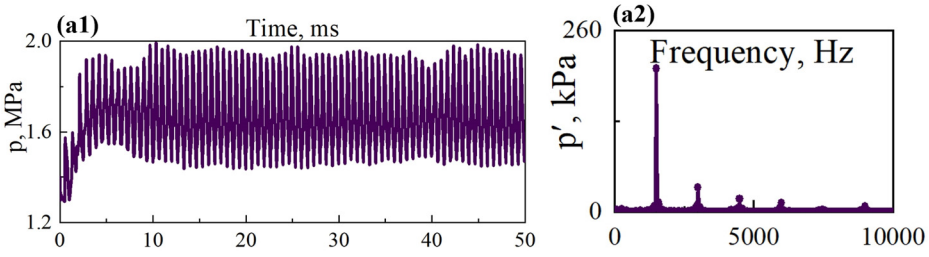

FIG. 15. Time trace of pressure monitored at Probe A1 and corresponding FFT results in CVRC.

TABLE IV. Comparison of the first three dominant frequencies of the acoustic pressure signal and their corresponding peak-to-peak oscillation amplitudes with experimental measurements.[25]

	Experimental measurement[28]		Simulation results		Error	
Acoustic mode	f, Hz	p'_{ptp}, kPa	f, Hz	p'_{ptp}, kPa	f	p'_{ptp}
1	1331	387	1500	411	12.7%	6.2%
2	2655	89	2999	70	12.9%	21.3%
3	3986	46	4499	38	12.8%	17.4%

12.7%, and the error in the peak-to-peak amplitude is 6.2%, indicating that the result accuracy meets the requirements of this study.

ACKNOWLEDGMENTS

This work was supported by the Fund-supported Project: the Key Programs of National Natural Science Foundation of China (No. U2241250).

AUTHOR DECLARATIONS

Conflict of Interest

The authors have no conflicts to disclose.

Author Contributions

Yuanzhe Liu: Conceptualization (equal); Data curation (equal); Formal analysis (equal); Investigation (lead); Methodology (lead); Software (lead); Validation (equal); Visualization (lead); Writing – original draft (lead). **Zhuopu Wang:** Conceptualization (equal); Investigation (equal); Writing – review & editing (equal). **Xiaoxin Wu:** Writing – review & editing (equal). **Yu Guan:** Supervision (equal); Writing – review & editing (equal). **Zhuyin Ren:** Writing – review & editing (equal). **Peijin Liu:** Conceptualization (equal); Funding acquisition (lead); Writing – review & editing (equal).

DATA AVAILABILITY

The data that support the findings of this study are available from the corresponding author upon reasonable request.

REFERENCES

[1]M. P. Juniper and R. I. Sujith, "Sensitivity and nonlinearity of thermoacoustic oscillations," Annu. Rev. Fluid Mech. **50**, 661–689 (2018).
[2]T. Poinsot, "Prediction and control of combustion instabilities in real engines," Proc. Combust. Inst. **36**(1), 1–28 (2017).
[3]W. A. Sirignano, "Driving mechanisms for combustion instability," Combust. Sci. Technol. **187**(1–2), 162–205 (2015).
[4]R. Sujith, M. Juniper, and P. Schmid, "Non-normality and nonlinearity in thermoacoustic instabilities," Int. J. Spray Combust. Dyn. **8**(2), 119–146 (2016).
[5]J. C. Oefelin and V. Yang, "Comprehensive review of liquid-propellant combustion instabilities in F-1 engines," J. Propul. Power **9**(5), 657–677 (1993).
[6]W. E. Anderson and V. Yang, *Liquid Rocket Engine Combustion Instability* (AIAA, 1995).
[7]D. Zhao, Z. L. Lu, H. Zhao, X. Y. Li, B. Wang, and P. J. Liu, "A review of active control approaches in stabilizing combustion systems in aerospace industry," Prog. Aeosp. Sci. **97**, 35–60 (2018).
[8]A. Urbano, L. Selle, G. Staffelbach, B. Cuenot, T. Schmitt, S. Ducruix, and S. Candel, "Exploration of combustion instability triggering using large eddy simulation of a multiple injector liquid rocket engine," Combust. Flame **169**, 129–140 (2016).
[9]L. Hakim, A. Ruiz, T. Schmitt, M. Boileau, G. Staffelbach, S. Ducruix, B. Cuenot, and S. Candel, "Large eddy simulations of multiple transcritical coaxial flames submitted to a high-frequency transverse acoustic modulation," Proc. Combust. Inst. **35**(2), 1461–1468 (2015).
[10]L. Hakim, T. Schmitt, S. Ducruix, and S. Candel, "Dynamics of a transcritical coaxial flame under a high-frequency transverse acoustic forcing: Influence of the modulation frequency on the flame response," Combust. Flame **162**(10), 3482–3502 (2015).
[11]K. Balasubramanian and R. Sujith, "Non-normality and nonlinearity in combustion-acoustic interaction in diffusion flames," J. Fluid Mech. **594**, 29–57 (2008).
[12]R. I. Sujith and V. R. Unni, "Complex system approach to investigate and mitigate thermoacoustic instability in turbulent combustors," Phys. Fluids **32**(6), 061401 (2020).
[13]K. Manoj, S. A. Pawar, J. Kurths, and R. I. Sujith, "Rijke tube: A nonlinear oscillator," Chaos **32**(7), 072101 (2022).
[14]V. Nair, G. Thampi, and R. I. Sujith, "Intermittency route to thermoacoustic instability in turbulent combustors," J. Fluid Mech. **756**, 470–487 (2014).
[15]L. Kabiraj and R. I. Sujith, "Nonlinear self-excited thermoacoustic oscillations: Intermittency and flame blowout," J. Fluid Mech. **713**, 376–397 (2012).
[16]Y. Guan, V. Gupta, and L. K. B. Li, "Intermittency route to self-excited chaotic thermoacoustic oscillations," J. Fluid Mech. **894**, R3 (2020).
[17]P. Kasthuri, I. Pavithran, S. A. Pawar, R. I. Sujith, R. Gejji, and W. Anderson, "Dynamical systems approach to study thermoacoustic transitions in a liquid rocket combustor," Chaos **29**, 103115 (2019).
[18]P. Kasthuri, S. A. Pawar, R. Gejji, W. Anderson, and R. I. Sujith, "Coupled interaction between acoustics and unsteady flame dynamics during the transition to thermoacoustic instability in a multi-element rocket combustor," Combust. Flame **240**, 112047 (2022).
[19]P. Kasthuri, A. Krishnan, R. Gejji, W. Anderson, N. Marwan, and R. I. Sujith, "Investigation into the coherence of flame intensity oscillations in a model multi-element rocket combustor using complex networks," Phys. Fluids **34**, 034107 (2022).
[20]C. Aoki, H. Gotoda, S. Yoshida, and S. Tachibana, "Dynamic behavior of intermittent combustion oscillations in a model rocket engine combustor," J. Appl. Phys. **127**(22), 224903 (2020).
[21]Y. Liu, P. Liu, Z. Wang, W. Ao, and Y. Guan, "Numerical investigation of combustion instability in a single-element liquid rocket engine: Intermittency routes before and after thermoacoustic instability," Aerosp. Sci. Technol. **143**, 108691 (2023).
[22]Y. Liu, P. Liu, Z. Wang, W. Ao, G. Xu, and Y. Guan, "Numerical investigation of combustion instability in a liquid rocket engine: Interaction effect between hydrodynamics and acoustic mode," Aerosp. Sci. Technol. **143**, 108711 (2023).
[23]Y. Liu, P. Liu, Z. Wang, W. Ao, and Y. Guan, "Large eddy simulation of combustion instability in a subcritical hydrogen peroxide/kerosene liquid rocket engine: Intermittency route to period-2 thermoacoustic instability," Phys. Fluids **35**, 065145 (2023).
[24]Y. Liu, P. Liu, Z. Wang, W. Ao, and Y. Guan, "Large eddy simulation of effects of oxidizer inlet temperatures on the transition routes before and after thermoacoustic instability in a subcritical hydrogen peroxide/kerosene liquid rocket engine," Phys. Fluids **35**(12), 125141 (2023).

[25]Y. Liu, Z. Wang, W. Ao, Y. Guan, and P. Liu, "Detached eddy simulation of the interaction between acoustics and flame dynamics during the transition before and after longitudinal thermoacoustic instability in a multi-element liquid rocket engine," Phys. Fluids **36**(6), 065150 (2024).
[26]Y. Guan, W. He, M. Murugesan, Q. Li, P. Liu, and L. K. B. Li, "Control of self-excited thermoacoustic oscillations using transient forcing, hysteresis and mode switching," Combust. Flame **202**, 262–275 (2019).
[27]Y. Yu, S. Koeglmeier, J. Sisco, and W. Anderson, "Combustion instability of gaseous fuels in a continuously variable resonance chamber (CVRC)," in 44th AIAA/ASME/SAE/ASEE Joint Propulsion Conference & Exhibit, AIAA Paper No. AIAA 2008-4657, 2008.
[28]M. E. Harvazinski, C. Huang, V. Sankaran, T. W. Feldman, W. E. Anderson, C. L. Merkle, and D. G. Talley, "Coupling between hydrodynamics, acoustics, and heat release in a self-excited unstable combustor," Phys. Fluids **27**(4), 045102 (2015).
[29]G. M. R. Tamanampudi, S. Sardeshmukh, W. Anderson, and C. Huang, "Combustion instability modeling using multi-mode flame transfer functions and a nonlinear Euler solver," Int. J. Spray Combust. Dyn. **12**(1), 1–24 (2020).
[30]Z. Shadram, T. M. Nguyen, A. Sideris, and W. A. Sirignano, "Physics-aware neural network flame closure for combustion instability modeling in a single-injector engine," Combust. Flame **240**, 111973 (2022).
[31]L. Selle, "Compressible large eddy simulation of turbulent combustion in complex geometry on unstructured meshes," Combust. Flame **137**(4), 489–505 (2004).
[32]Y. Sun, D. Zhao, C. Ji, T. Zhu, Z. Rao, and B. Wang, "Large-eddy simulations of self-excited thermoacoustic instability in a premixed swirling combustor with an outlet nozzle," Phys. Fluids **34**(4), 044112 (2022).
[33]L. Zhan, T. M. Nguyen, J. Xiong, F. Liu, and W. A. Sirignano, "Combustion dynamics of ten-injector rocket engine using flamelet progress variable," Combust. Flame **267**, 113538 (2024).
[34]X. Han, J. Li, and A. S. Morgans, "Prediction of combustion instability limit cycle oscillations by combining flame describing function simulations with a thermoacoustic network model," Combust. Flame **162**(10), 3632–3647 (2015).
[35]S. Iavarone, A. Péquin, Z. X. Chen, N. A. K. Doan, N. Swaminathan, and A. Parente, "An a priori assessment of the Partially Stirred Reactor (PaSR) model for MILD combustion," Proc. Combust. Inst. **38**(4), 5403–5414 (2021).
[36]K. Guo, Y. Ren, P. Chen, W. Lin, Y. Tong, and W. Nie, "Analysis of spontaneous longitudinal combustion instability in an O_2/CH_4 single-injector rocket combustor," Aerosp. Sci. Technol. **119**, 107209 (2021).
[37]W. Li, D. Zhao, X. Chen, Y. Sun, S. Ni, D. Guan, and B. Wang, "Numerical investigations on solid-fueled ramjet inlet thermodynamic properties effects on generating self-sustained combustion instability," Aerosp. Sci. Technol. **119**, 107097 (2021).
[38]T. M. Nguyen and W. A. Sirignano, "Spontaneous and triggered longitudinal combustion instability in a single-injector liquid-rocket combustor," AIAA J. **57**(12), 5351–5364 (2019).
[39]See www.openfoam.org for "The OpenFOAM Foundation" (2013).
[40]J. Li, Y. Xia, A. S. Morgans, and X. Han, "Numerical prediction of combustion instability limit cycle oscillations for a combustor with a long flame," Combust. Flame **185**, 28–43 (2017).
[41]Y. Liu, P. Liu, Z. Wang, G. Xu, and B. Jin, "Numerical investigation of mode competition and cooperation on the combustion instability in a non-premixed combustor," Acta Astronaut. **198**, 271–285 (2022).
[42]Y. Yalcinkaya and A. G. Gungor, "Pressure gradient effect on flame-vortex interaction in lean premixed bluff-body stabilized flames," Phys. Fluids **35**, 045105 (2023).
[43]B. Wu, X. Zhao, B. R. Chowdhury, B. M. Cetegen, C. Xu, and T. Lu, "A numerical investigation of the flame structure and blowoff characteristics of a bluff-body stabilized turbulent premixed flame," Combust. Flame **202**, 376–393 (2019).
[44]I. Celik, M. Klein, and J. Janicka, "Assessment measures for engineering LES applications," J. Fluids Eng. **131**, 031102 (2009).
[45]B. J. Geurts and J. Fröhlich, "A framework for predicting accuracy limitations in large-eddy simulation," Phys. Fluids **14**(6), L41–L44 (2002).
[46]I. B. Celik, Z. N. Cehreli, and I. Yavuz, "Index of resolution quality for large eddy simulations," J. Fluids Eng. **127**, 949 (2005).
[47]Y. Guan, B. Yin, Z. Yang, and L. K. B. Li, "Forced synchronization of self-excited chaotic thermoacoustic oscillations," J. Fluid Mech. **982**, A9 (2024).
[48]S. A. Pawar, M. Raghunathan, K. V. Reeja, P. R. Midhun, and R. I. Sujith, "Effect of preheating of the reactants on the transition to thermoacoustic instability in a bluff-body stabilized dump combustor," Proc. Combust. Inst. **38**(4), 6193–6201 (2021).
[49]J.-P. Eckmann, S. O. Kamphorst, and R. D. Ruelle, "Recurrence plots of dynamical systems," Europhys. Lett. **4**(9), 973–977 (1987).
[50]Y. Guan, P. Liu, B. Jin, V. Gupta, and L. K. B. Li, "Nonlinear time-series analysis of thermoacoustic oscillations in a solid rocket motor," Exp. Therm. Fluid Sci. **98**, 217–226 (2018).
[51]T. M. Nguyen and W. A. Sirignano, "The impacts of three flamelet burning regimes in nonlinear combustion dynamics," Combust. Flame **195**, 170–182 (2018).
[52]D. D. A. Rosenberg and J. F. Driscoll, "Flame index and its statistical properties measured to understand partially premixed turbulent combustion," Combust. Flame **162**, 2808–2822 (2015).
[53]Y. C. Yu, J. C. Sisco, S. Rosen, A. Madhav, and W. E. Anderson, "Spontaneous longitudinal combustion instability in a continuously-variable resonance combustor," J. Propul. Power **28**(5), 876–887 (2012).